CrossMark

Finding Strong Gravitational Lenses in the DESI DECam Legacy Survey

X. Huang[1], C. Storfer[1], V. Ravi[2], A. Pilon[1], M. Domingo[2], D. J. Schlegel[3], S. Bailey[3], A. Dey[4], R. R. Gupta[3], D. Herrera[4], S. Juneau[4], M. Landriau[3], D. Lang[5,6,7], A. Meisner[4], J. Moustakas[8], A. D. Myers[9], E. F. Schlafly[4], F. Valdes[4], B. A. Weaver[4], J. Yang[10], and C. Yèche[11]

[1] Department of Physics and Astronomy, University of San Francisco, San Francisco, CA 94117-1080, USA
[2] Department of Computer Science, University of San Francisco, San Francisco, CA 94117-1080, USA
[3] Physics Division, Lawrence Berkeley National Laboratory, 1 Cyclotron Road, Berkeley, CA 94720, USA
[4] National Optical Astronomy Observatory, 950 N. Cherry Ave., Tucson, AZ 85719, USA
[5] Dunlap Institute, University of Toronto, Toronto, ON M5S 3H4, Canada
[6] Department of Astronomy & Astrophysics, University of Toronto, Toronto, ON M5S 3H4, Canada
[7] Perimeter Institute for Theoretical Physics, Waterloo, ON N2L 2Y5, Canada
[8] Department of Physics and Astronomy, Siena College, 515 Loudon Rd., Loudonville, NY 12211, USA
[9] Department of Physics & Astronomy, University of Wyoming, 1000 E. University, Dept 3905, Laramie, WY 82071, USA
[10] Steward Observatory, University of Arizona, 933 N. Cherry Ave., Tucson, AZ 85721, USA
[11] IRFU, CEA, Université Paris-Saclay, F-91191 Gif-sur-Yvette, France

Abstract

We perform a semi-automated search for strong gravitational lensing systems in the 9000 deg^2 Dark Energy Camera Legacy Survey (DECaLS), part of the Dark Energy Spectroscopic Instrument Legacy Imaging Surveys. The combination of the depth and breadth of these surveys are unparalleled at this time, making them particularly suitable for discovering new strong gravitational lensing systems. We adopt the deep residual neural network architecture developed by Lanusse et al. for the purpose of finding strong lenses in photometric surveys. We compile a training sample that consists of known lensing systems in the Legacy Surveys and the Dark Energy Survey as well as non-lenses in the footprint of DECaLS. In this paper we show the results of applying our trained neural network to the cutout images centered on galaxies typed as ellipticals in DECaLS. The images that receive the highest scores (probabilities) are visually inspected and ranked. Here we present 335 candidate strong lensing systems, identified for the first time.

1. Introduction

Strong lensing systems (Walsh et al. 1979; Lynds & Petrosian 1986; Paczynski 1987; Soucail et al. 1987, 1988) have been used to study how dark matter is distributed in galaxies and clusters (e.g., Kochanek 1991; Koopmans & Treu 2002; Bolton et al. 2006; Koopmans et al. 2006; Vegetti & Koopmans 2009; Tessore et al. 2016). As a cosmological probe, time delays in multiply lensed quasars provide competitive constraints on the Hubble constant H_0 (e.g., Refsdal 1964; Blandford & Narayan 1992; Suyu et al. 2010, 2013; Treu & Marshall 2016; Bonvin et al. 2017; Wong et al. 2019) independent of the distance ladder approach.

In recent years, highly magnified, multiply imaged supernovae (SNe), both core-collapse (Kelly et al. 2015) and Type Ia (Quimby et al. 2014; Goobar et al. 2017), have been discovered. With their well-characterized brightness time evolution in optical and near-infrared wavelengths (the SN lightcurves), such strongly lensed SNe are ideally suited to measure time delays and H_0 in future surveys (e.g., Goldstein & Nugent 2017; Goldstein et al. 2019, 2018; Wojtak et al. 2019) .

In this paper we show that hundreds of new strong lensing systems can be found in the three band imaging data (grz) from the Dark Energy Spectroscopic Instrument (DESI) Legacy Surveys[12] (Dey et al. 2019). To find these lenses from a data set that covers one third of the sky, we adopt the residual neural network (He et al. 2015a, 2015b, 2016) developed by Lanusse et al. (2018), the winning algorithm of the Strong Gravitational Lens Finding Challenge (Metcalf et al. 2019), to automate the process as much as possible.

This paper is organized as follows. A brief description of the Legacy Surveys is given in Section 2. In Section 3, we describe our methodology and training sample. In Section 4, we show the inference results and present our best strong lensing system candidates. We discuss our results in Section 5, and conclude in Section 6.

2. Observations

The details of the DESI Legacy Imaging Surveys are described in Dey et al. (2019, D19). Here we present a brief summary. The Legacy Surveys consist of three projects: the Dark Energy Camera Legacy Survey (DECaLS), observed by the Dark Energy Camera (DECam; Flaugher et al. 2015) on the 4 m Blanco telescope at the Cerro Tololo Inter-American Observatory; the Beijing-Arizona Sky Survey (BASS), by the 90Prime camera (Williams et al. 2004) on the Bok 2.3 m telescope owned and operated by the University of Arizona located on Kitt Peak; and the Mayall z-band Legacy Survey (MzLS), by the Mosaic3 camera (Dey et al. 2016) on the 4 m Mayall telescope at Kitt Peak National Observatory. Together they will ultimately cover ∼14,000 deg^2 of the extragalactic sky visible from the northern hemisphere in grz bands, with a 5σ z-band median limiting magnitude of 22.5 mag for galaxies with an exponential disk profile with $r_{i,\mathrm{half}} = 0{.}''45$.

---

[12] legacysurvey.org
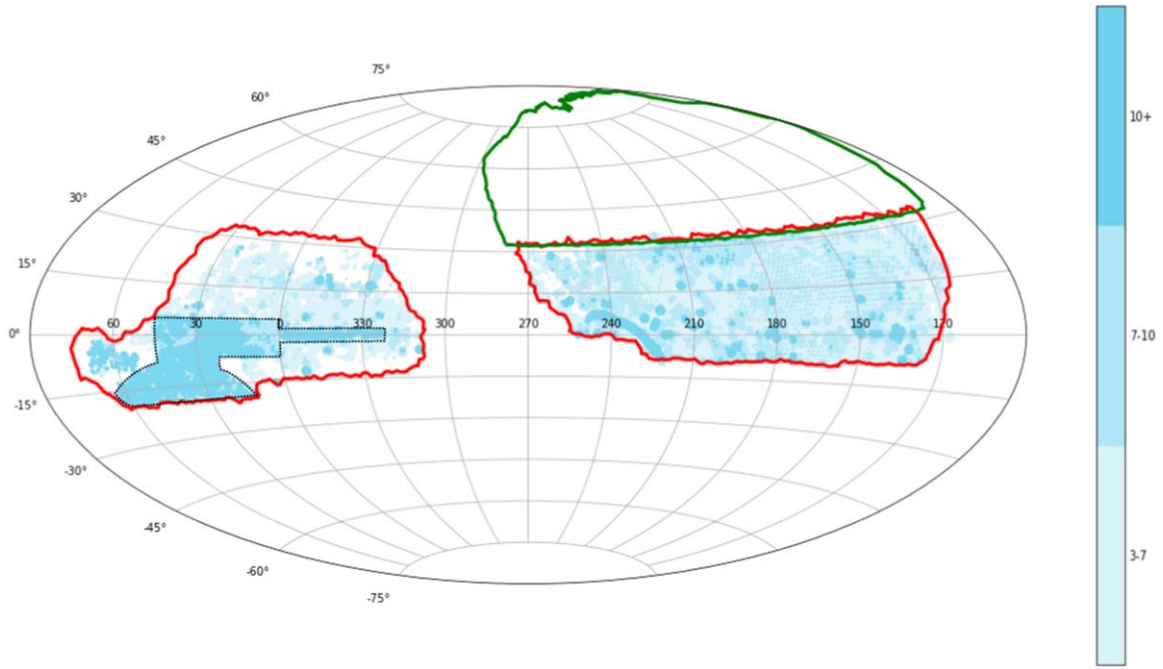
Figure 1. DESI Legacy Surveys footprint in an equal area Aitoff projection in equatorial coordinates with the DECaLS and MzLS/BASS regions highlighted with red and green outlines, respectively. Above the Galactic plane, there is a small amount of overlap between the surveys. For DECaLS, patches with different shades of blue indicate the depth in z band: light blue for between three and seven passes; medium blue, between seven and ten; and dark blue, greater than ten. We left the MzLS/BASS region blank because in the paper we have not searched for lenses in that region. Note that observations in grz bands of the northern part (decl. $> -30°$) of the Dark Energy Survey (DES; black dotted outline) are included in DECaLS.

The combined survey footprint is split into two contiguous areas by the Galactic plane. DECaLS covers the $\sim$9000 deg^2 $\delta \lesssim +32°$ sub-region of the Legacy Surveys. Figure 1 shows the different regions in the the Legacy Surveys footprint and the depth of the z-band observation for DR7, which is indicative of the completeness of the survey.

For DECaLS, the delivered image quality has a FWHM of approximately 1.29, 1.18, 1″11 for g, r, and z bands respectively. The MzLS has imaged the $\delta \gtrsim +32°$ (NGC) footprint of the Legacy Surveys in z-band that complemented the BASS g- and r-band observations in the same sub-region. While the delivered image quality of MzLS has a median seeing of $\approx$1″01, the median FWHMs for BASS are 1″61 and 1″47 in the g- and r-bands, respectively. We choose here to focus on DECaLS due to its better gr seeing than BASS. However, we intend in future work to apply the machine-learning framework we have developed for DECaLS to the northern BASS/MzLS area, by possibly incorporating transfer learning, active learning, or domain adaption (e.g., Tzeng et al. 2017) techniques.

The Legacy Surveys used the Tractor package (Lang et al. 2016) as a forward-modeling approach to perform source extraction on pixel-level data. Tractor takes as input the individual images from multiple exposures in multiple bands, with different seeing in each. After source detection, the point source ("PSF") and spatially extended ("REX," round exponential galaxy) models are computed for every source and the better of these two is used when deciding whether to keep the source. The spatially extended sources (REX) are further classified if χ^2 is improved by 9 by treating it as a deVaucouleurs (DEV), an exponential (EXP) profile, or a composite of DEV + exponential (COMP).[13] The same light

profile (EXP, DEV, or COMP) is consistently fit to all images in order to determine the best-fit source shape parameters and photometry.

The categories of DEV and COMP indicate the classification of elliptical galaxies. Given that the vast majority of lensing events are caused by early-type galaxies, we decided to target only objects with DEV and COMP classifications in this paper.

3. The Training Sample and Residual Neural Networks

3.1. Training Sample

Deep convolutional neural networks (CNNs) and their variations have been shown to be highly effective in image recognition. In recent years, this technique has been successfully applied to recognize instances of strong lenses in simulations (e.g., Metcalf et al. 2019, and references therein). In previous applications of CNNs to real observations, training samples are constructed from simulated lens images, combined with observed (Petrillo et al. 2017), simulated (Jacobs et al. 2017; Pourrahmani et al. 2018), or a mixture of observed and simulated non-lenses (Jacobs et al. 2019). This is because the number of known lenses, on the order of several hundred, is thought to be too small to effectively train CNN models. We note that the data set for Jacobs et al. (2017) is from the Canada–France–Hawaii Telescope (CFHT) Legacy Survey; Petrillo et al. (2017), the Kilo Degree Survey (de Jong et al. 2015); Pourrahmani et al. (2018), the Hubble Space Telescope ACS i-band observations of the Cosmological Evolution Survey (COSMOS; Capak et al. 2007) field; and Jacobs et al. (2019), the Dark Energy Survey (DES; The Dark Energy Survey Collaboration 2005). All of these searches were performed on completed surveys.

We decided to use only observed data for lenses and non-lenses in our training sample for partial deployment on

---

[13] http://legacysurvey.org/dr7/description/
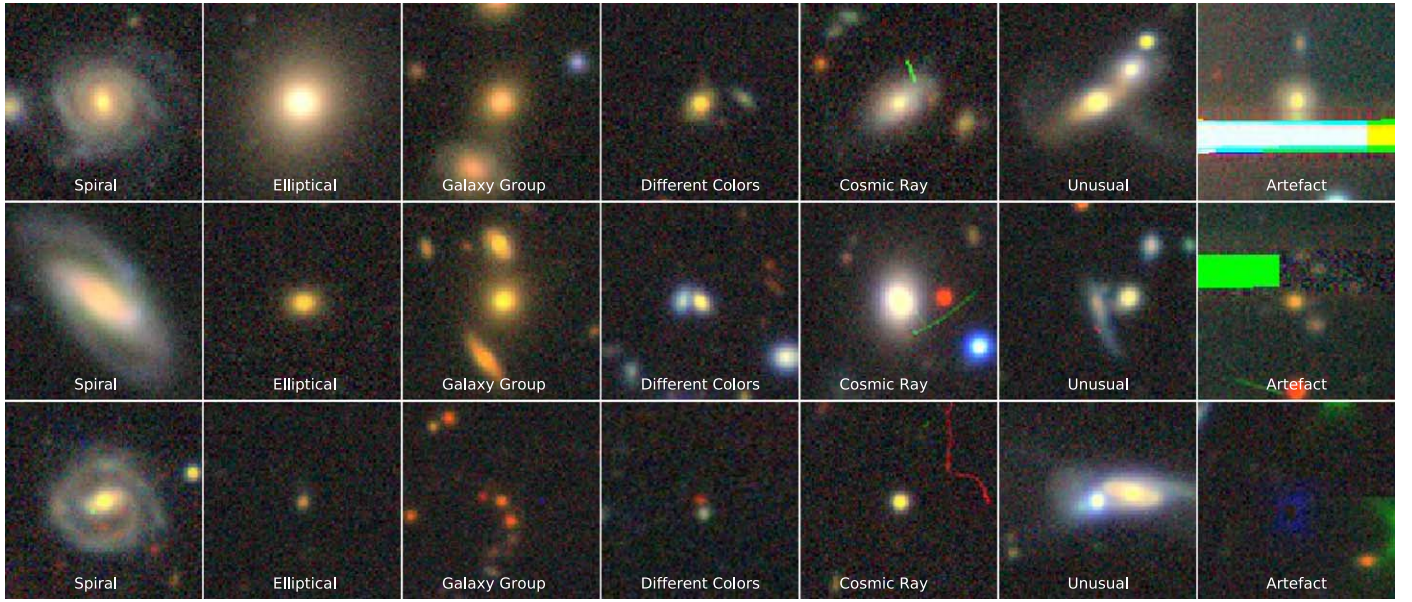
Figure 2. Examples of non-lens images in the training sample selected by eye. In order, the seven columns show the categories of (see text): spiral galaxies, ellipitcal galaxies, galaxy groups, galaxies with different colors, cosmic rays, unusual configurations, and finally data reduction artefacts.

DECaLS, which is near completion, and have obtained encouraging results. We identify the known lenses in the Legacy Surveys and DES DR1. A catalog of known lenses in the Legacy Surveys is also necessary in order to identify new lens candidates. Both DECaLS and DES used DECam (see D19). DES has *grizY* observations with greater depths (see Figure 1) in the three bands common with Legacy Surveys. Due to the paucity of lenses, we have used known strong lenses in all of Legacy Surveys, while in this paper we will focus on finding new lenses only in the DECaLS footprint. The Master Lens Database[14] (Moustakas et al. 2012), which contains hundreds of lensing events up to 2016, provided the initial list for the lens training sample. We have since added several hundred more lenses and lens candidates from more recent publications (Carrasco et al. 2017; Diehl et al. 2017; Jacobs et al. 2017, 2019; Pourrahmani et al. 2018; Sonnenfeld et al. 2018; Wong et al. 2018). In total we have identified ∼700 previously known lenses or lens candidates in the Legacy Surveys and DES. A number of these systems were discovered spectroscopically or through imaging with better seeing and/or greater depth than the Legacy Surveys and DES. Some of them therefore have subarcsecond deflection angles and/or lensed sources fainter than can be clearly seen from the DECaLS and DES observations. Through human inspection, we deem 613 as discernible lenses in the Legacy Surveys (199) and DES (414) footprints. For the lenses in the DES footprint, we only include *grz* bands. We also assemble 13,000 non-lens image cutouts from the Legacy Surveys, all with at least three passes in each of the *grz* bands. Of these, 5000 are galaxies categorized as DEV or COMP in D19 (see Section 2), which are elliptical galaxies, and another 5000 of all types of galaxies. For both cases, we apply a *z*-band magnitude cut of 22.5 mag. Given that on average we expect one strong lens in $\mathcal{O}(10^4)$ galaxies (e.g., Oguri & Marshall 2010), incidental inclusion of a lens or two in these randomly selected galaxies is not a significant concern.

The reason for including non-elliptical galaxies is to provide more non-lens configurations for the neural net. Two of the co-authors have also selected another 3000 non-lenses by eye so as to cover as many non-lens configurations as possible, especially cases that can potentially be confused by the neural net. These include spiral galaxies of different sizes and spiral arm configurations, elliptical galaxies, galaxy groups, images having objects with different colors (typically a blue galaxy next to a red one), cosmic rays appearing in different bands (some of which have curved trajectories), unusual arrangements of galaxies or stars, and finally certain data reduction artefacts (Figure 2). Simulated non-lenses typically do not cover these scenarios.

3.2. Residual Neural Networks

We have adopted the Residual Neural Network (ResNet) model of Lanusse et al. (2018, L18),[15] which used Theano[16] and Lasagne[17] libraries. We re-implemented their model in TensorFlow,[18] in part because major development for Theano ceased after the 1.0 release on 2017 November 15. We test the translated ResNet model using the simulated training set from the Strong Gravitational Lens Finding Challenge (Metcalf et al. 2019) and have reproduced the results in L18, which was the winning entry for the Lens Challenge. The architecture of the model is described in detail in L18.

L18 has provided much guidance to our approach. At this stage we have left their architecture and hyperparameters unchanged, including the batch size (128), total number of training epochs (120), pre-processing of the images, and data augmentation (random rotation, mirroring, and zooming within a range of [0.9, 1.0]; for details, see Section 3.3 of L18). The lens and non-lens images in the training sample are cutouts with a dimension of 101×101 pixels, following the specification in the Lens Challenge.

---

[14] http://admin.masterlens.org/index.php

[15] https://github.com/McWilliamsCenter/CMUDeepLens
[16] http://deeplearning.net/software/theano/
[17] https://github.com/Lasagne/Lasagne
[18] https://www.tensorflow.org/

We split the training sample into training, validation, and testing sets, with ratios of 70:20:10. The sizes of our training, validation, and testing sets are then, respectively, 9876 (423), 2818 (118), and 1427 (72) where the values in parentheses are the number of lenses. We set aside a testing set because we want to leave open the possibility of varying the architecture and hyperparameters to optimize the neural net's performance. We then train the ResNet on the supercomputer Cori[19] at the National Energy Research Scientific Computing Center (NERSC),[20] using three Haswell computing nodes, [21] one worker each. The 120 epochs of training took 17 hr. The distributed training was accomplished by using Horovod.[22] Performing distributed training with deep (46 layers in this case; L18) neural networks can be non-trivial. We experimented with different numbers of decay epochs and found that with three workers, a decay epoch of 40 (i.e., the learning rate of the ResNet is decreased by a factor 10 every 40 epochs of training) works the best.

The ResNet attempts to minimize the cross entropy loss function:

$$-\sum_{i=1}^{N} y_i \log \hat{y}_i + (1 - y_i)\log(1 - \hat{y}_i) \tag{1}$$

where y_i is label for the ith image (1 for lens and 0 for non-lens), and $\hat{y}_i \in [0, 1]$ is the model predicted probability.

While the loss function is monitored during the training process to determine the point of termination, the overall performance of the trained model is typically assessed by the Receiver Operating Characteristic (ROC) curve. The ROC curve shows the True Positive Rate (TPR) versus the False Positive Rate (FPR) for the validation set, where P(ositive) indicates a lens and N(egative), a non-lens. With the definitions TP = correctly identified as a lens, False Positive = incorrectly identified as a lens, True Negative = correctly rejected, and False Negative = incorrectly rejected,

$$\text{TPR} = \frac{\text{TP}}{\text{P}} = \frac{\text{TP}}{\text{TP} + \text{FN}}$$

and

$$\text{FPR} = \frac{\text{FP}}{\text{N}} = \frac{\text{FP}}{\text{FP} + \text{TN}}.$$

The curve is generated by gradually increasing the threshold probability for a positive identification from 0 to 1. Random classifications will result in a diagonal line in this space with an area under the ROC curve (or AUC) equal 0.5. For a perfect classifier, AUC = 1.

The decision of using three nodes was based on our experience with a smaller training set. We can significantly shorten the training time by employing six or more nodes. Since the training set has a total of 9876 images, with a batch size of 128 images and 3 workers, it takes 26 steps to complete one full training epoch.

In Figure 3, left panel, we show how the cross entropy loss functions vary as training progresses. For the validation set, we show the value at every epoch. For the training set, the cross

[19] https://docs.nersc.gov/systems/cori/
[20] https://www.nersc.gov/
[21] https://docs.nersc.gov/systems/cori/#haswell-compute-nodes
[22] https://github.com/horovod/

entropy was reported for every step, which we have boxcar smoothed with a window size of 26. As L18 also noted, the loss function (Equation (1)) and the AUC for the validation set both plateau well within 120 epochs of training. Since the model has performed well, we have left the architecture and hyperparameters in L18 unchanged and moved directly to deployment. Thus, so far we have not used the validation set, or the testing set, for training.

We achieve an AUC of 0.98 for the validation set (Figure 3, right panel). Even though our training and validation sets contain far fewer lenses, our AUC matches the performance on simulated data in L18.

4. Results

4.1. Inference and Lens Candidates

We apply our trained ResNet model to 5.7 million DEV and COMP type galaxies in DECaLS with at least three passes in each of the three bands (*grz*) and *z*-band magnitude ⩽20.0. This magnitude cut was chosen because it includes 92% of the known lenses in the Legacy Surveys and results in a manageable number of images for human inspection.

Four co-authors (A. P., C. S., M. D., and V. R.) have inspected ∼50,000 cutout images that receive a probability ⩾0.9, evenly split. They select candidates according to these criteria, erring on the generous side: small blue galaxy/galaxies (red galaxies are rare but certainly acceptable) next to the red galaxy/galaxies at the center that

1. are typically 1″–5″ away
2. have low surface brightness
3. curve toward the red galaxy/galaxies
4. have counter/multiple images with similar colors (especially in Einstein-cross like configuration)
5. are elongated (including semi- or nearly full circles).

Typically, most candidates do not have all these characteristics. In general, the greater the number of characteristics listed above an image has, the higher they are ranked by humans. A fifth co-author (X. H.), in consultation with another co-author (R. G.), examines all these "first pass" candidates and assigns the grades of A, B, and C, and discards the rest:

1. Grade A: we have a high level of confidence of these candidates. Many of them have one or more prominent arcs, usually blue. The rest have one or more clear arclets, sometimes arranged in counter-image configurations with similar colors (again, typically blue). However, there are clear cases with red arcs.
2. Grade B: they have similar characteristics as the Grade As. For the cutout images where there appear to be giant arcs they tend to be fainter than those for the Grade As. Likewise, the putative arclets tend to be smaller and/or fainter, or isolated (without counter images).
3. Grade C: they generally have features that are even fainter and/or smaller than what is typical for the Grade B candidates, but that are nevertheless suggestive of lensed arclets. They are usually without counter images, except for a few cases. In almost all cases, if these are indeed lensing systems, the deflection angles are comparable to or only slightly larger than the seeing.
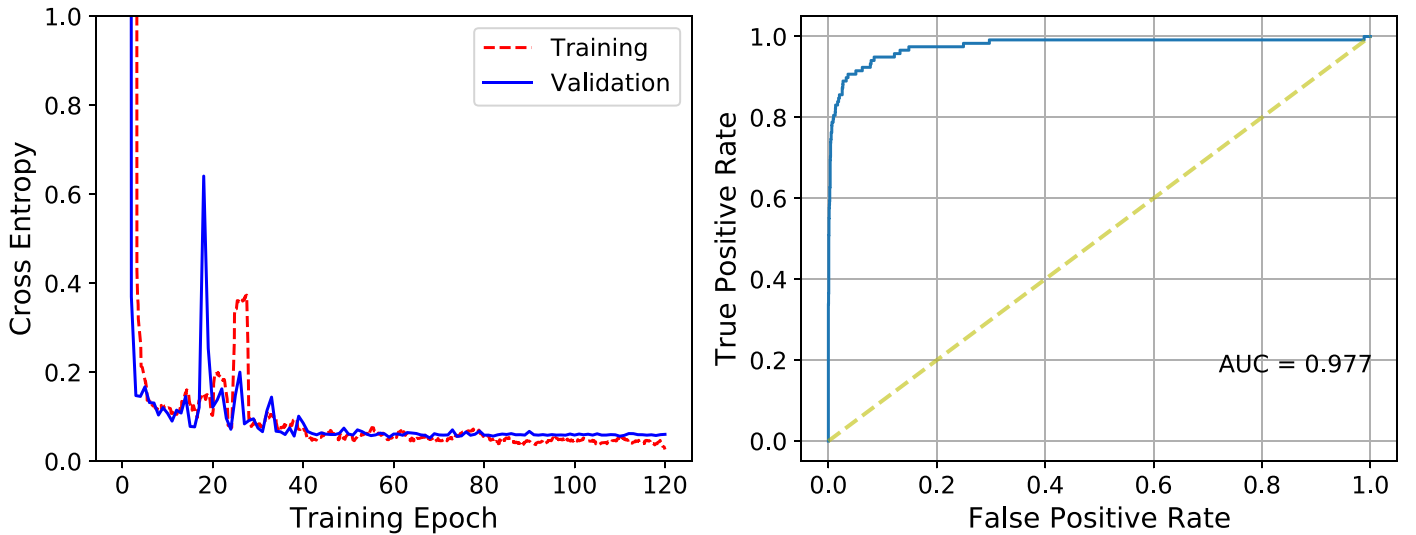
For Grade B and C candidates, we have included a few cases where it is difficult to judge whether it is a lensing event versus a coincidental placement of galaxies, a spiral galaxy, or a ring

Figure 3. Left: the cross entropy loss functions for the training and validation sets over 120 epochs. Right: the receiver operative characteristic (ROC) curve for the validation set with the area under the curve (AUC) = 0.98.

galaxy. In total we have identified 342 candidates: 60 As, 106 Bs, and 176 Cs, listed in Tables 1–3 and shown in Figures 4–6. The locations of the candidates in the sky are shown in Figure 7.

We have checked our candidates against the HST Source Catalog (HSCv3),[23] and found six known lenses among the Grade A candidates: DESI-016.3319+01.7490 and DESI-026.2679−04.9310 (Stark et al. 2013), DESI-036.1436 −00.0411 (Gladders et al. 2003), DESI-168.2943+23.9443 (Kubo et al. 2009), DESI-204.0002−03.5250 and DESI-219.7907+12.1404 (SDSS DR12 brightest cluster galaxy; Sharon et al. 2020). A seventh, DESI-038.2078-03.3906 (Stark et al. 2013), was pointed out to us during the peer review process (by Chien-Hsiu Lee at NOAO after the paper was posted on the arXiv). These are not in our training sample, and are shown with a red rim in Figure 4. This leaves the number of new Grade A candidates as 53, and the total number of new lens candidates, 335.

We have found at least 13 new cluster/group scale strong lenses: DESI-019.6618-05.4441, DESI-060.2420-13.9567, DESI-167.8517+14.1473 DESI-219.9855+32.8402, and DESI-359.8897+02.1399 (with a giant red arc) among Grade A, and DESI-009.9772-12.2100, DESI-018.1714-19.0457, DESI-022.3389+00.6547, DESI-023.6765+04.5639, DESI-061.1134-17.2082, DESI-154.7654+17.0697, DESI-202.3729 +31.3290, and DESI-216.1003+25.2423 among Grade B candidates.

Among the hundreds of galaxy scale candidates, there are many notable lensing events. We especially would like to highlight: DESI-135.3125+09.940, a system having a lens with $g - r = 3.3$, likely indicating a high redshift (e.g., Jacobs et al. 2019); DESI-041.5205-06.1275, a nearly perfect Einstein cross; and DESI-155.7366-05.0529, with a red arc, which would have a redshift of ~4 if it is a Lyman-break galaxy.

We would like to emphasize the importance of the Grade B and C candidates. The "rediscovered lenses" outside the training sample are in the A category (7 out of 60). This is not a surprise: typically having brighter arcs with larger deflection angles, these systems are comparatively easy to find.

Higher redshift lensing systems from ground-based surveys are likely not in the Grade A category but in B or C. The current known lensing sample mostly consists of luminous elliptical galaxies at redshifts from approximately 0.4 to 0.8 (e.g., Brownstein et al. 2012; Wong et al. 2018). Our lens candidates are fainter, and mostly have optical and infrared colors consistent with $z > 0.8$ (e.g., Jacobs et al. 2019). Higher lens redshifts significantly increase the power relative to lower redshift samples for constraining the mass function of low-mass CDM halos, due to the greater optical depth for perturbations by low-mass halos associated with a longer path length along the line of sight (Despali et al. 2018; Ritondale et al. 2019). In addition, the lensed sources will tend to have higher redshifts than in known lensing systems as well.

Finally, we checked our candidate list against the spectroscopic database from SDSS I and II (York et al. 2000), SDSS III/BOSS (Eisenstein et al. 2011), and SDSS IV/ eBOSS (Blanton et al. 2017) and found 121 matches, which is slightly greater than one third of all candidates. The available redshifts are included in Tables 1–3.

The completeness is difficult to estimate at this point, even just for elliptical galaxies because (1) the data reduction for the Legacy Survey has not completed (recall for this deployment, we have only included images with at least three passes in each band), and (2) we have not run inference on the REX category.

4.2. Probability Bins Lower than 0.9

It is notable that there are typically many more candidates with probability greater than 0.9 than with probabilities between 0.8 and 0.9. In a small testing inference run that covers ≈4% of the DECaLS footprint, we have examined and found lens candidates with probability <0.9. The yield typically rapidly diminishes with lower probabilities. As stated earlier, for the deployment on galaxy morphological types DEV and COMP, we impose a magnitude cut at $z \leqslant 20.0$ mag. For our small test inference run, we included all objects with $z \leqslant 22.5$ mag. From that run, we have found one Grade B lens (DESI-135.9714+07.1954) with a z-band magnitude of 20.87.

Given that a strong majority of the best lens candidates are from the probability >0.9 bin for the categories of DEV and

Table 1
Grade A Candidates

Name	Type	mag_g	mag_r	mag_z	Probability	z	Survey
DESI-011.5084-01.9412	DEV	20.94	19.19	17.97	0.936	0.5501	BOSS
DESI-015.8164+00.0823	DEV	19.64	18.08	17.21	1.000	0.2662	SDSS
DESI-016.3319+01.7490	DEV	19.95	18.17	17.27	0.987	0.3612	BOSS
DESI-016.5230+00.5463	DEV	21.52	19.66	18.25	1.000	0.5941	BOSS
DESI-018.1074+02.3773	DEV	21.27	19.35	18.12	0.948	0.5039	BOSS
DESI-019.4949-05.4550	DEV	21.41	19.66	18.37	0.984	0.5797	BOSS
DESI-019.6618-05.4441	DEV	22.30	20.38	18.99	0.969		
DESI-022.7106-16.0024	COMP	19.44	18.64	17.61	0.948		
DESI-024.1631+00.1384	COMP	18.83	17.18	16.29	0.998	0.3441	SDSS
DESI-025.2755-17.2232	DEV	20.43	18.96	17.62	0.989		
DESI-026.1390-11.7026	COMP	20.09	18.39	17.00	0.961		
DESI-026.2679-04.9310	COMP	20.75	19.67	18.43	0.998		
DESI-026.4848+04.0413	DEV	22.29	20.78	19.05	0.927		
DESI-027.3284-13.8180	DEV	22.13	20.95	19.22	0.998		
DESI-027.9723-14.8069	DEV	21.62	20.51	18.90	1.000		
DESI-029.6032-00.6665	DEV	21.05	19.45	17.94	0.918	0.5970	SDSS
DESI-030.2832-15.8547	DEV	21.12	19.26	18.16	0.997		
DESI-031.1712-15.0266	DEV	20.08	18.35	17.40	0.996		
DESI-036.1436-00.0411	DEV	21.67	20.33	18.78	0.962	0.7846	eBOSS
DESI-036.4422-07.6274	DEV	20.98	19.08	17.89	0.990	0.5138	BOSS
DESI-037.0378-12.8812	DEV	20.39	19.01	17.92	0.997		
DESI-038.2078-03.3906	DEV	20.08	18.39	17.40	0.999		
DESI-040.3034-00.9646	DEV	19.27	17.83	17.02	0.999	0.2418	SDSS
DESI-040.3168-06.5372	DEV	20.63	18.94	17.96	0.997		
DESI-041.5205-06.1275	DEV	23.97	21.99	19.92	0.999		
DESI-060.1043-16.3979	DEV	19.05	17.88	17.16	0.987		
DESI-060.2420-13.9567	DEV	21.07	19.54	18.11	0.931		
DESI-122.0852+10.5284	DEV	19.94	18.14	17.10	0.997	0.4754	SDSS
DESI-133.5531-04.4026	DEV	21.80	20.45	18.72	0.849		
DESI-133.6197+10.1374	DEV	19.06	17.44	16.57	0.989	0.2978	SDSS
DESI-135.3125+09.9401	COMP	24.28	20.96	18.89	0.993		
DESI-137.8568+14.2991	DEV	20.61	18.80	17.51	0.969	0.5464	BOSS
DESI-140.8110+18.4954	DEV	20.20	19.60	18.65	0.875	0.8732	BOSS
DESI-141.0626+05.7690	DEV	21.17	19.48	17.98	0.952	0.6128	BOSS
DESI-143.3887+09.3219	DEV	22.16	20.41	18.71	0.999	0.7430	BOSS
DESI-145.9507+00.9906	COMP	20.53	18.97	17.90	1.000		
DESI-152.0763+31.7005	COMP	21.23	19.45	18.18	0.991	0.5394	SDSS
DESI-154.6972-01.3590	DEV	20.53	18.72	17.79	1.000	0.3883	BOSS
DESI-155.7366-05.0529	DEV	20.64	19.00	17.54	0.987		
DESI-160.2351-01.0663	DEV	17.80	16.33	15.51	0.942	0.2502	SDSS
DESI-162.4577+05.7749	DEV	18.76	17.37	16.55	0.997	0.2640	SDSS
DESI-165.6876+12.1864	DEV	23.23	21.46	19.36	0.983		
DESI-168.2943+23.9443	DEV	17.44	15.82	14.95	0.968	0.3361	SDSS
DESI-186.3033-00.4390	COMP	19.49	18.17	17.44	0.987		
DESI-186.8292+17.4324	COMP	21.56	19.95	19.01	0.903		
DESI-189.5370+15.0309	DEV	20.38	18.69	17.37	0.998		
DESI-194.5344+03.5358	DEV	19.90	18.29	17.31	0.989	0.4279	BOSS
DESI-202.6690+04.6707	DEV	18.84	17.21	16.33	0.987	0.3363	SDSS
DESI-204.0002-03.5250	EXP	21.36	21.12	20.37	0.900	0.1764	SDSS
DESI-213.6664+19.4787	DEV	19.05	17.34	16.09	0.993	0.5768	BOSS
DESI-214.6278+25.1814	DEV	17.83	16.23	15.41	0.986	0.2909	SDSS
DESI-215.2654+00.3719	DEV	21.32	20.05	18.73	0.974		
DESI-216.8280-06.7541	DEV	18.64	17.14	16.34	0.972		
DESI-216.9538+08.1792	DEV	20.83	19.16	17.99	0.960	0.5338	BOSS
DESI-219.7907+12.1404	DEV	20.54	18.60	17.59	0.863	0.4273	SDSS
DESI-219.9855+32.8402	DEV	19.65	17.84	16.87	0.812	0.4176	SDSS
DESI-318.0376-01.7568	DEV	18.14	16.73	15.92	0.974	0.2241	BOSS
DESI-319.3483-00.9478	DEV	20.05	18.20	17.17	0.935	0.4272	SDSS
DESI-349.5492-11.1012	COMP	19.51	17.78	16.12	0.980		
DESI-359.8897+02.1399	DEV	18.94	17.04	16.05	0.993	0.4295	BOSS

Note. 33 of the above 60 Grade A lens candidates have spectroscopic redshifts from SDSS (see text). All redshift uncertainties $< 3.7 \times 10^{-4}$.

Table 2
Grade B Candidates

Name	Type	mag_g	mag_r	mag_z	Probability	z	Survey
DESI-005.6187+01.8037	DEV	20.93	20.09	18.59	0.889		
DESI-009.1701+00.7687	DEV	21.91	20.44	18.82	0.964		
DESI-009.9772-12.2100	DEV	21.93	20.06	18.91	0.900		
DESI-010.2401-09.0954	COMP	21.70	20.14	18.99	0.990		
DESI-010.2876-00.7303	DEV	21.33	19.67	18.40	0.898	0.5633	SDSS
DESI-010.3630-01.1298	DEV	29.52	22.73	20.78	0.909		
DESI-011.0219-04.8058	DEV	23.15	21.10	19.20	0.896	0.7715	eBOSS
DESI-011.9235-06.1032	DEV	22.45	20.55	19.34	0.815		
DESI-012.5310-18.6438	DEV	19.43	17.72	16.85	0.929		
DESI-014.0105+03.0152	DEV	22.19	20.35	19.07	0.970	0.5367	BOSS
DESI-014.0683-01.3924	DEV	20.16	18.96	17.75	0.989		
DESI-014.0730-02.4262	DEV	20.98	19.34	18.41	0.994		
DESI-014.4452-16.7457	DEV	21.64	19.79	18.56	1.000		
DESI-014.6199-00.4627	DEV	21.53	20.40	19.21	0.951		
DESI-015.0641-00.2718	COMP	21.00	19.31	18.33	1.000	0.4287	SDSS
DESI-015.0721+00.0027	DEV	20.04	18.53	17.75	0.958	0.2758	BOSS
DESI-015.2668-17.5344	COMP	20.63	19.31	18.41	0.997		
DESI-015.2991+00.1673	DEV	21.55	19.97	18.99	0.985		
DESI-015.3533-17.0192	DEV	22.03	20.28	19.11	0.902		
DESI-015.3806+00.5700	DEV	22.56	20.98	19.40	0.987		
DESI-015.4415+03.2399	DEV	20.93	19.42	18.39	0.968	0.5518	BOSS
DESI-015.5430-00.3184	DEV	21.43	20.10	18.83	1.000	0.6376	BOSS
DESI-015.6201-00.4207	DEV	20.71	19.09	18.21	0.998		
DESI-015.6531-00.0963	COMP	20.75	19.11	18.21	1.000	0.3675	BOSS
DESI-015.9831+00.3187	DEV	21.19	19.79	18.50	1.000	0.6205	BOSS
DESI-016.1439-00.5185	COMP	18.66	17.01	16.14	1.000	0.3453	SDSS
DESI-016.2119+00.4207	DEV	21.19	19.64	18.54	0.998	0.5293	BOSS
DESI-016.2273+00.0668	DEV	19.58	18.07	17.19	0.999	0.2757	SDSS
DESI-016.2921-18.3895	DEV	22.46	20.76	19.31	0.972		
DESI-016.3969+00.1169	COMP	18.93	17.53	16.76	0.990		
DESI-016.5355-00.2139	DEV	18.28	17.16	16.42	0.922	0.1971	SDSS
DESI-016.7876+01.2914	DEV	20.25	18.39	17.41	0.999	0.4217	BOSS
DESI-016.8597+03.2136	COMP	17.84	16.25	15.35	0.977	0.3245	BOSS
DESI-016.9695-14.4480	DEV	21.30	19.38	18.07	0.999		
DESI-017.0297-03.5796	DEV	19.77	18.34	17.54	0.985		
DESI-017.4350-14.6600	DEV	21.17	19.54	18.02	0.995		
DESI-017.5240-02.5417	COMP	19.31	17.49	16.53	0.933	0.4312	BOSS
DESI-018.0754-04.5830	COMP	21.38	19.78	18.64	0.993	0.5290	BOSS
DESI-018.1714-19.0457	DEV	20.58	18.93	17.49	0.999		
DESI-018.2548-03.7210	DEV	20.00	18.34	17.45	0.992	0.3156	BOSS
DESI-018.4039-18.9942	DEV	21.48	19.86	18.80	0.963		
DESI-020.4712-17.9274	COMP	19.49	17.72	16.26	0.925		
DESI-020.7598-13.2227	DEV	22.60	20.83	19.25	0.936		
DESI-022.3389+00.6547	DEV	22.85	21.29	19.64	0.992		
DESI-023.6765+04.5639	DEV	20.93	19.03	17.70	0.951	0.5508	BOSS
DESI-029.0400-10.4926	COMP	22.79	21.24	19.85	0.999		
DESI-034.9916-14.9460	DEV	22.88	21.30	19.64	0.927		
DESI-035.0816-04.1971	DEV	19.83	18.39	17.63	0.994		
DESI-035.7821-05.4661	DEV	22.21	20.37	19.23	0.999	0.4963	BOSS
DESI-036.0677-16.3767	DEV	21.45	19.75	18.36	0.987		
DESI-036.2542-05.6058	DEV	21.13	19.29	18.34	0.978	0.4381	BOSS
DESI-036.3915-05.0365	DEV	19.25	18.14	17.43	0.998		
DESI-036.4490-15.0922	DEV	21.60	20.11	18.71	0.959		
DESI-037.0236-05.2927	COMP	20.58	19.48	18.77	0.999		
DESI-038.9951-06.0696	DEV	22.83	20.96	19.60	0.988		
DESI-040.5720-16.4116	DEV	21.02	19.15	17.76	0.939		
DESI-040.7053-00.5888	DEV	22.08	20.22	19.24	1.000	0.4119	BOSS
DESI-040.8111-00.1499	DEV	22.19	20.21	18.50	1.000	0.7167	BOSS
DESI-041.4742-00.7052	DEV	21.23	20.09	19.39	1.000		
DESI-041.9391-00.5247	DEV	21.25	19.38	18.06	1.000	0.5801	SDSS
DESI-046.4723-14.8812	DEV	23.96	21.67	19.60	0.946		
DESI-047.7087-17.7748	DEV	22.51	20.93	19.45	0.950		
DESI-047.7647-13.2341	DEV	19.33	18.58	17.59	0.957		
DESI-060.0471-15.8799	DEV	22.22	21.54	19.85	0.971		

Table 2
(Continued)

Name	Type	mag_g	mag_r	mag_z	Probability	z	Survey
DESI-060.8033-15.2161	COMP	22.54	20.82	19.33	0.993		
DESI-060.8089-15.0458	DEV	22.06	20.65	19.41	0.993		
DESI-061.1134-17.2082	DEV	22.61	20.68	18.72	0.999		
DESI-061.1909-14.5760	COMP	18.53	16.70	15.76	0.921		
DESI-063.6323-04.5427	DEV	20.36	18.74	17.87	0.990		
DESI-131.3607+00.0361	DEV	24.15	21.79	19.70	0.800		
DESI-134.0057-07.2488	DEV	19.55	17.84	16.87	0.990		
DESI-135.9714+07.1954	DEV	25.90	23.38	20.87	0.900		
DESI-140.8863+20.3278	DEV	20.77	19.04	18.06	0.873		
DESI-143.0565-05.6041	DEV	21.45	19.61	18.51	0.866		
DESI-144.1511+08.8633	COMP	20.53	18.79	17.25	0.987		
DESI-144.4242+31.4659	COMP	19.16	17.56	16.27	0.949	0.5969	BOSS
DESI-144.6321-04.2535	COMP	21.15	19.36	18.03	0.921		
DESI-145.0099+05.4279	DEV	21.35	20.12	18.86	0.900		
DESI-150.0945+00.0047	COMP	18.92	18.64	18.18	1.000		
DESI-150.8860-02.9493	DEV	20.89	18.95	17.36	0.992	0.6817	BOSS
DESI-154.5307-00.1368	DEV	20.38	18.59	17.68	0.943	0.3718	SDSS
DESI-154.7654+17.0697	COMP	18.73	17.16	16.32	0.939	0.3013	BOSS
DESI-155.4865+11.2037	DEV	19.83	18.62	17.82	0.995		
DESI-157.9622+01.7544	COMP	20.34	18.78	17.77	0.989		
DESI-158.7893-02.3037	COMP	22.13	20.39	18.82	0.996		
DESI-167.8517+14.1473	DEV	17.82	16.44	15.65	0.904	0.2211	SDSS
DESI-170.6983+25.2669	DEV	20.00	18.11	17.12	0.983	0.4310	SDSS
DESI-192.0242-06.5158	COMP	17.68	16.12	15.26	0.983		
DESI-194.5900+15.6322	DEV	22.41	20.50	18.86	0.977	0.6847	BOSS
DESI-194.8376+11.6490	COMP	19.62	18.33	17.51	0.935		
DESI-201.7783+02.2129	DEV	20.33	18.81	17.98	0.636		
DESI-201.7841-02.2996	COMP	21.79	19.97	18.25	0.931	0.7441	BOSS
DESI-202.3729+31.3290	DEV	21.30	19.64	18.67	0.989		
DESI-204.1663-05.7814	DEV	20.06	18.31	17.37	0.991		
DESI-204.6057+28.3294	DEV	20.92	19.32	18.02	1.000	0.5841	BOSS
DESI-211.0927+02.7242	DEV	21.47	19.83	18.92	0.951		
DESI-216.1003+25.2423	DEV	20.53	19.06	18.27	0.989	0.2325	BOSS
DESI-217.1429-07.0963	DEV	20.02	18.48	17.62	0.938		
DESI-217.4784+12.0433	DEV	21.54	19.98	18.74	0.942	0.5531	BOSS
DESI-219.0374-01.3295	DEV	20.10	18.66	17.60	0.847		
DESI-219.9228+00.5073	DEV	18.67	17.67	17.00	0.837	0.1377	SDSS
DESI-241.0592+06.4200	DEV	20.93	19.70	18.93	0.999		
DESI-241.5432+14.1008	COMP	19.99	18.38	17.43	0.989		
DESI-317.3884+05.1456	COMP	21.71	19.56	18.10	0.976	0.5642	BOSS
DESI-328.5453+00.6329	COMP	18.81	17.62	16.92	0.998		
DESI-351.4891-00.8741	DEV	23.36	21.27	19.52	0.982		

Note. 37 of the above 106 Grade B lens candidates have spectroscopic redshifts from SDSS (see text). All redshift uncertainties $< 3.7 \times 10^{-4}$.

COMP, in this paper we focus on this subset for human inspection.

A rough estimate of completeness can be performed by checking how many lensing systems from the validation (118) and testing (72) set would be "rediscovered." This depends on the threshold. 77 of the 190 lenses in the validation and testing sets received a probability of >0.9, or about 40%. The precision (TP/(TP+FP)) versus recall (TP/(TP + FN), or completeness) curve for the validation and testing sets, with probability threshold values marked, are shown in Figure 8.

The implication seems to be that there are hundreds more lenses to be discovered in lower probability bins. We can already confirm there are good lens candidates with probability below 0.9 based on visual inspection for a small subset of the data. However, we caution against a simple forecast based on these percentages. The images in the training sample that receive low probability often are less obvious lenses for the

human inspector. In fact for the next round of training, we would remove some of them from the training sample.

To demonstrate, in Figure 9, we show four examples of DECaLS images of lensing systems in the current training sample that we would consider for removal. Without prior knowledge, these images could not have been determined to be lenses by visual inspection. The first three are from the Strong Lensing Legacy Survey (SL2S; Cabanac et al. 2007; More et al. 2012). This survey was carried out on the CFHT in *urgiz* bands and the lensing systems were found from both their WIDE and DEEP components. They ran semi-automated searches (More et al. 2012) on their *g*-band images, which are ~1.5 mag deeper than the 5σ *g*-band depth of DECaLS, and has a mean seeing of 0.″78. The DEEP fields were almost 10 times deeper. Therefore some of the blue arcs in the SL2S images are barely visible in their DECaLS counterparts, either due to the shallower *g*-band depth (Figure 9, Panels (a) and (b))

Table 3
Grade C Candidates

Name	Type	mag_g	mag_r	mag_z	Probability	z	Survey
DESI-005.7434+00.1667	DEV	21.28	20.92	20.37	0.835		
DESI-009.9958+00.5677	DEV	21.03	19.43	18.25	0.989	0.5255	SDSS
DESI-010.2439-02.0572	DEV	20.22	19.19	18.57	0.917		
DESI-013.5957-05.7105	DEV	21.44	19.59	18.44	0.961	0.5036	BOSS
DESI-013.9264-01.0692	DEV	20.54	19.17	18.29	0.982		
DESI-013.9873-00.6495	DEV	21.16	19.61	18.38	0.973	0.5659	SDSS
DESI-014.6980+00.2355	DEV	21.83	20.16	19.24	0.996		
DESI-014.7160-00.3509	COMP	18.77	17.67	16.99	0.997	0.2399	SDSS
DESI-015.0586+01.8480	DEV	20.54	18.81	17.88	0.934	0.4046	BOSS
DESI-015.1785-18.8779	DEV	21.37	19.92	19.14	0.908		
DESI-015.1912+03.7221	COMP	20.21	18.37	17.43	0.970	0.3979	BOSS
DESI-015.2403-16.9542	COMP	19.98	18.72	17.92	0.922		
DESI-015.2570-17.7561	DEV	21.28	19.40	18.18	0.991		
DESI-015.3628-00.9079	COMP	21.16	19.28	18.18	0.901	0.4635	SDSS
DESI-015.3792-03.3438	COMP	19.82	18.69	17.99	0.962		
DESI-015.8070-17.7531	DEV	20.75	18.99	18.07	0.931		
DESI-015.9669-18.0271	DEV	21.10	19.46	18.53	0.987		
DESI-016.1507-00.5780	DEV	21.26	19.72	18.79	0.990		
DESI-016.1763-02.4491	COMP	22.77	20.87	18.88	0.936		
DESI-016.1889-00.5809	DEV	21.79	20.10	19.26	0.990		
DESI-016.2032-06.6226	DEV	21.65	19.85	18.86	0.973		
DESI-016.2995-00.0690	DEV	21.93	20.32	19.27	0.994		
DESI-016.3200+00.9163	DEV	21.36	19.78	18.85	0.923		
DESI-016.4625+02.8614	DEV	21.49	19.84	18.87	0.913		
DESI-016.4883-00.1774	COMP	22.85	21.02	19.35	0.992		
DESI-016.5355-00.2139	DEV	18.28	17.16	16.42	0.922	0.1971	SDSS
DESI-016.8009-16.8580	DEV	20.94	19.41	18.53	0.901		
DESI-016.8554-00.7320	COMP	20.47	19.00	17.61	0.976		
DESI-016.9199-05.3919	DEV	21.30	19.64	18.44	0.970	0.5214	BOSS
DESI-016.9228-03.8680	COMP	21.06	19.46	18.18	0.979		
DESI-016.9682+00.3567	COMP	19.59	17.97	17.09	1.000	0.3133	SDSS
DESI-017.2362-17.9241	DEV	21.44	19.79	19.01	0.924		
DESI-018.0415+00.1861	DEV	19.67	18.29	17.50	0.916		
DESI-018.4701+03.4968	DEV	22.37	20.52	19.23	0.996	0.5517	BOSS
DESI-019.8976-12.8253	DEV	21.96	20.12	18.95	0.945		
DESI-020.3517+00.1654	DEV	21.01	19.92	18.75	0.971	0.7690	BOSS
DESI-020.5273-04.8117	DEV	21.20	19.36	18.40	0.985	0.3978	BOSS
DESI-021.5439-00.5883	DEV	21.33	19.79	18.95	0.985		
DESI-021.8518-05.7560	DEV	21.75	20.15	19.11	0.944		
DESI-021.9637+00.0975	DEV	21.43	20.15	19.39	0.967		
DESI-022.6104-15.3370	DEV	21.47	19.70	18.37	0.980		
DESI-023.6659-06.9344	COMP	22.22	20.65	19.76	0.921		
DESI-023.7790+01.5306	DEV	22.82	21.13	19.60	0.921		
DESI-024.7012-07.5349	DEV	21.38	19.67	18.61	0.975	0.4924	BOSS
DESI-025.8361-10.0680	COMP	19.79	18.67	17.97	0.980	0.2422	SDSS
DESI-026.2451-01.5934	DEV	22.38	20.80	19.62	0.905		
DESI-026.2771-00.7284	COMP	20.29	19.39	17.97	0.949		
DESI-027.5388-12.3284	DEV	20.88	19.15	18.28	0.926		
DESI-027.8872-08.5764	COMP	21.94	20.07	18.71	0.945	0.5735	BOSS
DESI-028.2710-09.8289	DEV	22.48	20.66	19.27	0.972	0.5973	BOSS
DESI-028.3093-00.4385	DEV	22.39	21.07	19.39	0.958		
DESI-028.8348-13.9044	COMP	20.24	19.28	18.71	0.900		
DESI-029.1778-10.1834	DEV	22.01	20.90	19.47	1.000		
DESI-030.8114-09.1587	DEV	20.11	18.62	17.87	1.000		
DESI-031.8778-14.8046	DEV	24.15	21.92	20.34	0.954		
DESI-033.9735-12.6841	DEV	21.85	20.04	18.87	0.992		
DESI-034.0253-04.5771	DEV	22.25	20.46	19.29	1.000		
DESI-034.3281-05.1331	DEV	23.33	21.65	20.26	0.993		
DESI-035.7202-03.9575	COMP	22.69	21.50	19.82	1.000	0.8368	eBOSS
DESI-035.8285-04.3979	DEV	21.41	19.72	18.80	0.937		
DESI-035.8379-07.3794	COMP	19.89	17.97	16.63	0.995		
DESI-035.8438-06.3246	COMP	20.05	18.32	17.47	0.967	0.3560	BOSS
DESI-035.8660-18.4836	COMP	18.51	16.97	16.16	0.954		
DESI-035.9027-06.8806	COMP	19.97	18.58	17.43	0.999		

Table 3
(Continued)

Name	Type	mag_g	mag_r	mag_z	Probability	z	Survey
DESI-035.9185-05.8453	DEV	22.43	21.00	19.88	0.996		
DESI-035.9393-04.4005	DEV	20.12	18.53	17.62	1.000	0.3037	BOSS
DESI-036.0184-04.4084	DEV	21.71	20.19	19.39	1.000		
DESI-036.0256-06.4796	DEV	21.58	20.29	19.47	0.986		
DESI-036.0536-06.1645	DEV	20.81	19.19	18.34	0.979		
DESI-036.0653-05.8029	DEV	22.90	21.55	19.62	0.998		
DESI-036.0879+00.0726	COMP	19.59	18.29	17.52	0.959		
DESI-036.1151-05.2254	DEV	22.06	21.00	19.61	0.998	0.9028	eBOSS
DESI-036.1457-05.4990	DEV	21.98	20.87	19.50	0.991		
DESI-036.2194-04.3486	DEV	22.68	21.65	19.95	1.000		
DESI-036.2244-06.3029	DEV	22.39	20.74	19.54	0.956		
DESI-036.2714-06.8192	DEV	19.62	18.92	18.38	0.983		
DESI-036.3530-04.6792	DEV	19.01	17.48	16.67	1.000	0.2643	BOSS
DESI-036.3795-04.2093	DEV	22.97	21.32	19.65	1.000	0.7726	eBOSS
DESI-036.4031-04.2550	DEV	22.08	20.32	19.05	1.000	0.5557	BOSS
DESI-036.4081-05.2473	DEV	20.63	19.04	18.17	0.999		
DESI-036.4268-05.1548	DEV	19.80	18.63	17.94	1.000		
DESI-036.4827-16.8621	DEV	19.41	17.99	17.14	0.984		
DESI-036.6282-04.6316	DEV	22.26	20.51	19.22	1.000	0.5906	BOSS
DESI-036.6556-03.7101	DEV	22.13	20.56	19.43	0.999		
DESI-036.6760-03.6801	DEV	20.33	19.05	18.21	1.000		
DESI-036.6777-03.6555	COMP	21.80	20.40	19.82	1.000		
DESI-036.6819-03.6905	DEV	21.02	19.39	18.53	1.000	0.3284	eBOSS
DESI-036.7198+00.2833	DEV	19.91	18.32	17.33	0.996	0.3022	SDSS
DESI-036.7325-05.1276	DEV	21.73	19.87	18.76	1.000	0.4361	BOSS
DESI-036.8076-05.0255	DEV	22.14	20.88	19.90	0.999		
DESI-036.8133-03.9033	COMP	19.64	18.88	18.15	0.999		
DESI-036.9560-06.1539	DEV	21.46	19.67	18.69	0.932	0.4324	BOSS
DESI-037.0345-04.5015	DEV	22.20	20.50	19.45	1.000		
DESI-037.1686-04.0027	DEV	20.09	18.75	18.01	1.000		
DESI-037.2011-04.1161	DEV	20.17	19.28	18.67	0.993	0.1406	BOSS
DESI-037.2064-01.2158	DEV	21.05	19.64	18.34	0.984	0.6895	BOSS
DESI-037.2945+03.7522	DEV	24.56	22.05	19.98	0.945		
DESI-037.4766+03.1089	DEV	22.26	20.84	19.46	0.985		
DESI-038.2709-10.4498	DEV	22.03	20.38	19.19	0.957		
DESI-038.8461-10.5125	DEV	20.76	19.29	18.51	0.964		
DESI-039.0463-06.3428	DEV	22.71	21.00	19.42	0.973		
DESI-039.2003+03.3583	DEV	20.93	19.31	18.25	0.984	0.4673	BOSS
DESI-039.9261-01.4632	DEV	19.68	18.51	17.68	0.957		
DESI-040.6372-12.1891	DEV	19.92	17.98	17.00	0.999		
DESI-040.6769-00.6487	DEV	23.64	21.84	19.95	0.968		
DESI-040.7046+02.2423	DEV	19.69	18.72	18.07	0.942		
DESI-040.8745-01.9373	DEV	23.10	21.18	19.68	1.000		
DESI-041.3678-01.2016	DEV	21.65	20.27	18.97	1.000	0.6669	BOSS
DESI-041.4318-08.6492	COMP	21.44	20.05	18.64	0.999	0.7261	BOSS
DESI-041.5548-00.7524	COMP	22.47	21.24	19.80	0.997		
DESI-041.7915-08.4225	DEV	21.39	19.50	18.31	0.957	0.5221	BOSS
DESI-041.9910-00.7425	DEV	21.70	20.45	19.68	0.999		
DESI-042.2156-00.5329	DEV	19.33	18.02	17.22	0.995	0.2547	BOSS
DESI-042.9152-00.5600	DEV	22.07	20.10	18.70	1.000	0.5846	BOSS
DESI-046.6993-15.0593	DEV	22.53	20.97	19.64	0.985		
DESI-047.3321-13.5368	DEV	22.19	20.49	19.21	0.998		
DESI-060.4389-14.7568	DEV	20.04	18.57	17.77	0.986		
DESI-060.6860-15.7303	COMP	19.67	18.89	18.30	0.976		
DESI-061.0991-14.3883	COMP	22.79	21.03	18.97	0.954		
DESI-064.4878-03.6133	DEV	19.04	17.83	17.07	0.997		
DESI-125.6392-00.4650	DEV	21.11	19.20	17.94	0.951	0.5253	BOSS
DESI-131.8556+14.2550	COMP	19.98	18.67	17.89	0.841		
DESI-138.6664-00.0821		22.79	21.03	19.69	0.953		
DESI-149.1942+00.7137	DEV	21.93	20.48	19.35	0.998		
DESI-150.2022+01.6538	DEV	18.52	17.20	16.45	0.998		
DESI-150.4045+02.5544	DEV	19.56	18.11	17.32	0.991	0.2477	BOSS
DESI-151.2006-03.7158	DEV	20.00	18.64	17.92	0.911		
DESI-151.7664+02.1430	DEV	20.51	18.84	17.95	0.972		

Table 3
(Continued)

Name	Type	mag_g	mag_r	mag_z	Probability	z	Survey
DESI-151.9855+02.4052	DEV	21.90	20.17	18.97	0.943	0.5307	BOSS
DESI-152.5264-01.9658	DEV	22.31	20.50	19.43	0.993		
DESI-152.8042-02.0432	DEV	17.72	16.39	15.62	0.965		
DESI-153.0462-00.8142	COMP	20.91	20.00	18.72	0.983		
DESI-154.3116+02.4885	DEV	19.42	17.68	16.73	0.999	0.3576	SDSS
DESI-155.4226+00.6966	DEV	22.48	20.58	19.12	0.919	0.6186	BOSS
DESI-158.0944+15.8846	DEV	21.57	20.03	18.45	0.949		
DESI-158.8311-00.5674	DEV	19.48	17.85	16.94	0.992	0.3157	SDSS
DESI-170.8533+15.1850	DEV	19.04	17.36	16.46	0.987	0.3406	BOSS
DESI-176.2181+08.9457	DEV	21.36	19.55	18.44	0.943	0.4971	BOSS
DESI-180.0490-00.4182	COMP	23.41	21.54	19.96	0.971		
DESI-181.9442+27.6152	COMP	18.56	17.04	16.20	0.995	0.3282	SDSS
DESI-184.3703+15.6730	DEV	21.69	20.21	19.05	0.942		
DESI-193.6112-08.7744	DEV	20.42	18.85	17.94	0.991		
DESI-201.4063+04.1883	DEV	20.87	19.50	18.65	0.455		
DESI-203.3751-02.1804	DEV	21.52	20.00	18.90	0.947		
DESI-204.7174-08.3381	DEV	20.36	18.83	18.03	0.743		
DESI-205.7370+22.6135	DEV	21.04	19.69	18.63	0.813	0.5198	BOSS
DESI-210.3880+13.3370	DEV	20.12	18.83	18.05	0.856		
DESI-212.6868-07.1025	DEV	20.45	19.12	18.34	0.942		
DESI-240.0759+05.6966	DEV	21.18	19.44	18.52	0.995		
DESI-240.3397+05.0773	DEV	21.87	20.91	19.89	0.981		
DESI-240.4006+05.5796	DEV	20.43	18.97	18.21	0.993		
DESI-240.5350+06.0657	DEV	22.56	20.99	19.66	1.000		
DESI-240.7203+06.5371	COMP	21.62	19.97	18.67	0.997		
DESI-241.2494+06.8555	DEV	21.68	20.27	19.36	0.999		
DESI-241.3833+15.8226	COMP	19.76	18.27	17.22	0.969	0.5119	BOSS
DESI-241.7841+07.0210	DEV	20.76	20.04	19.41	0.969		
DESI-241.8463+07.1753	COMP	21.47	19.49	18.04	1.000	0.5903	BOSS
DESI-242.0285+03.8786	DEV	22.07	21.07	19.44	0.909		
DESI-242.4262+06.1599	DEV	22.07	20.20	18.97	0.996	0.5453	BOSS
DESI-249.9825+19.0354	COMP	20.72	18.84	17.40	0.921	0.6064	BOSS
DESI-251.0765+01.6752	DEV	21.32	19.46	18.41	0.921		
DESI-251.1722+04.9724	DEV	20.45	18.90	17.99	0.901		
DESI-317.2431+03.9841	COMP	19.70	18.96	18.34	0.957		
DESI-319.7989+00.0575	DEV	20.16	18.79	18.00	0.958		
DESI-338.0990+01.5111	DEV	22.37	20.79	19.51	0.992		
DESI-351.1264-11.6503	DEV	21.83	19.94	18.55	1.000		
DESI-351.1287-11.2566	COMP	21.80	20.75	19.72	0.998		
DESI-351.1413-12.4955	DEV	20.75	18.92	17.98	1.000		
DESI-351.2285-11.6281	DEV	21.89	20.09	19.11	0.999		
DESI-351.2576-12.7728	DEV	24.17	22.08	19.89	0.997		
DESI-351.3096-12.5492	COMP	20.71	19.13	18.29	1.000		
DESI-351.3891-12.0013	DEV	20.74	19.38	18.59	0.998		
DESI-351.4008-11.9943	DEV	21.19	19.36	18.44	0.998		
DESI-351.4290-12.2431	DEV	20.59	18.78	17.88	1.000		
DESI-351.4915-11.6013	DEV	20.47	19.17	18.41	0.998		
DESI-351.5372-11.3464	DEV	21.76	20.16	19.38	0.999		

Note. 51 of the above 176 Grade C lens candidates have spectroscopic redshifts from SDSS (see text). All redshift uncertainties $< 3.9 \times 10^{-4}$.

and/or the comparatively inferior seeing of DECaLS (Figure 9, Panel (c)). The fourth example in Figure 3 (Panel (d)) comes from the Hyper Suprime-Cam Subaru Strategic Program (HSC-SSP; Aihara et al. 2018). Observed in *grizy* bands, this survey also has greater depth and better seeing than DECaLS. As a result, some of the blue arcs seen in the HSC images (Sonnenfeld et al. 2018) are barely visible in DECaLS.

From the experience of this deployment, we believe including images like these in the training sample has resulted in a number of images with high probability that cannot be unambiguously classified by visual inspection. These images significantly decrease the efficiency of human inspection

without clear improvement for completeness. This intuition seems to be correct from our preliminary results using an updated training sample. In the future, we will also experiment with getting cutout images directly from the SL2S and HSC surveys.

4.3. Human Inspection Efficiency

Below we briefly discuss the human inspection efficiency of the ResNet results thus far. In total we have examined ~50,000 objects. On average, 1 in 150 of the objects with probability from the ResNet model is deemed a lens candidate through
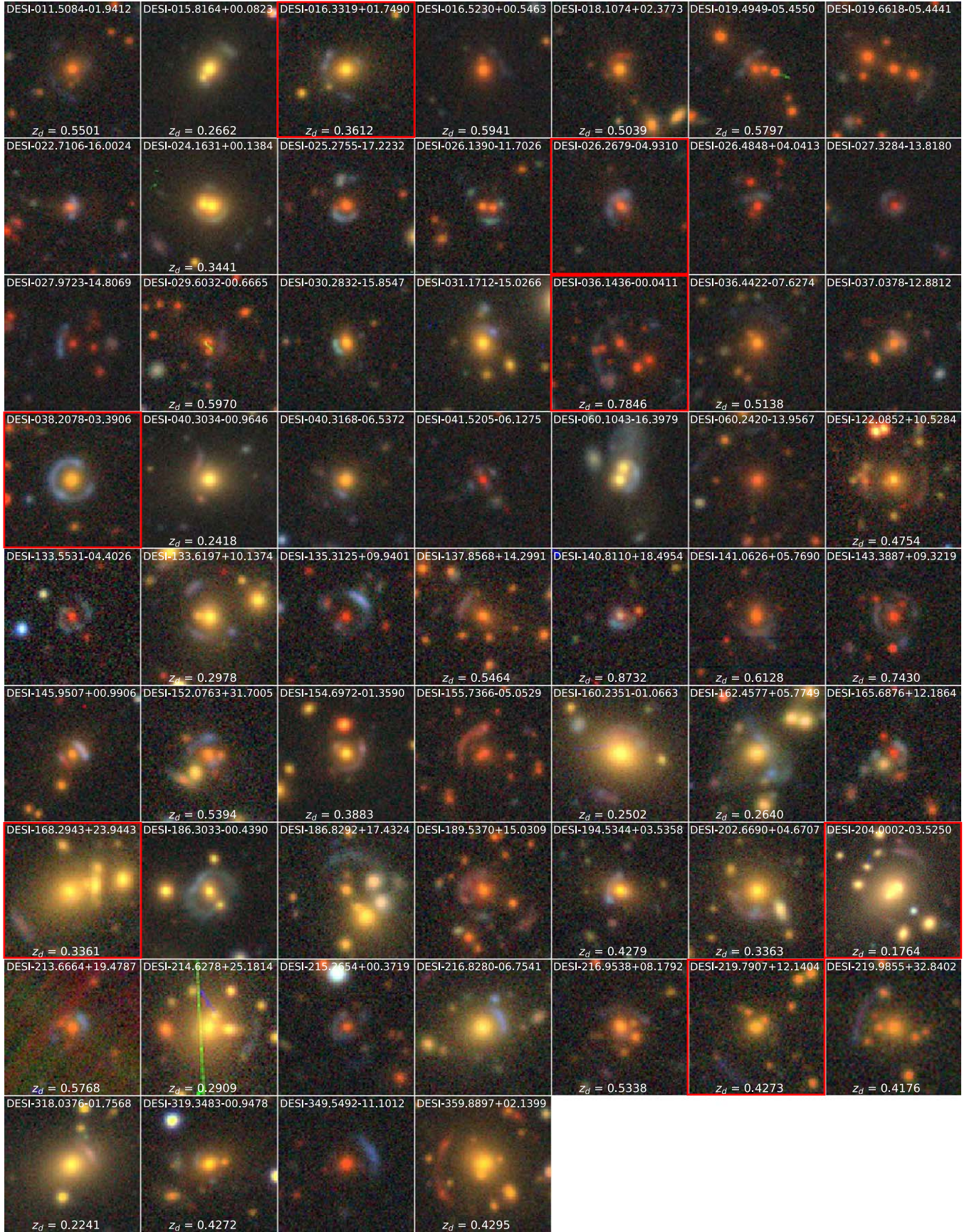
Figure 4. 60 Grade A lens candidates arranged in ascending R.A. Each image is 101 pixels $\approx 26\rlap{.}{''}2$ on the side, with N up and E to the left. The exception is DESI-204.0002-03.5250, which is 151 pixel $\approx 40\rlap{.}{''}3$ on the side. The seven images with a red rim are later found to be known lenses (see text). These seven lenses were not included in our training sample, and they happen to be in the selected subset of the Legacy Surveys data of 5.7 million elliptical galaxies.
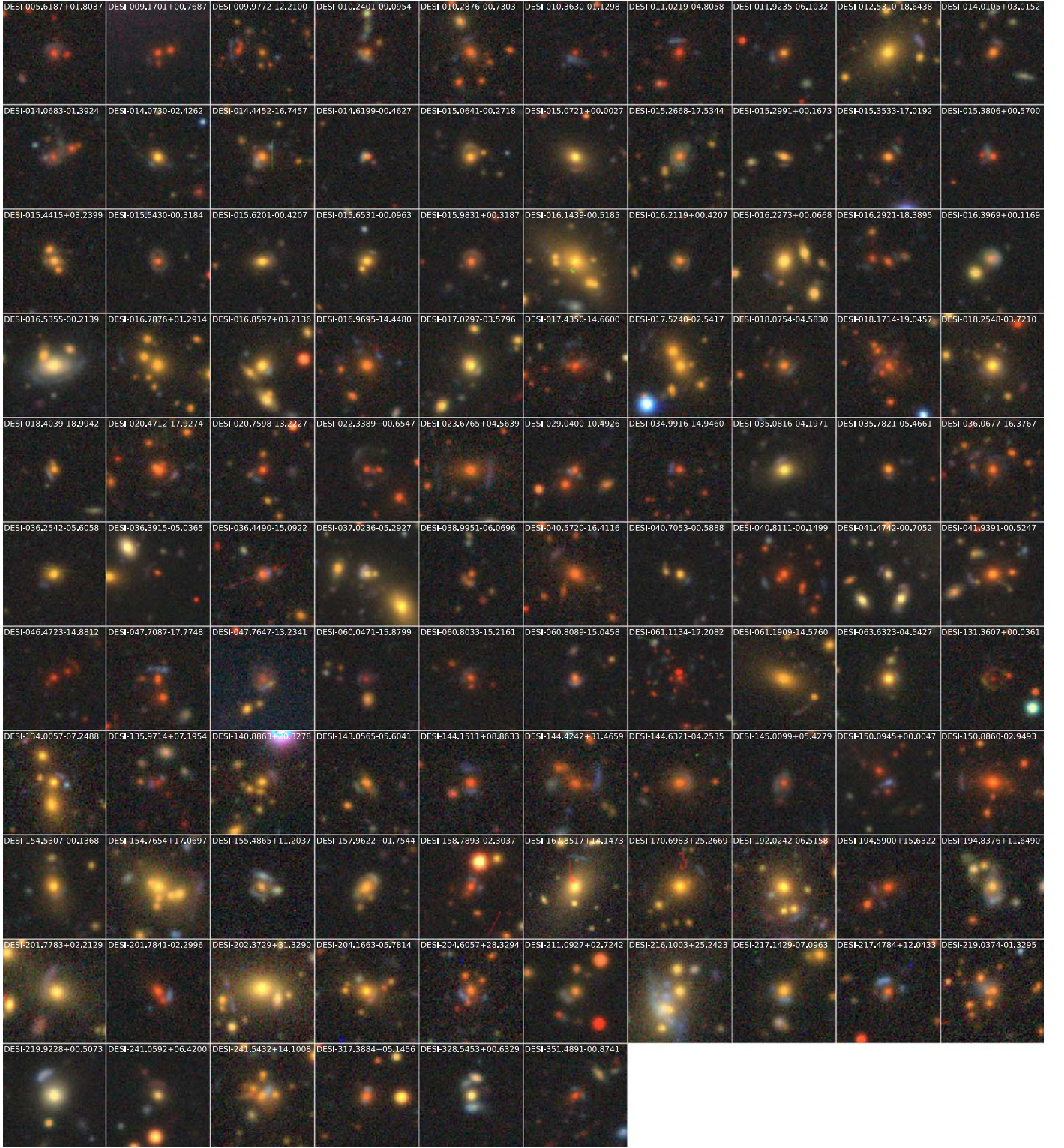
Figure 5. 106 Grade B lens candidates. Each image is 101 pixels ≈26″2 on the side, with N up and E to the left. The exceptions are DESI-009.9772-12.2100, DESI-061.1134-17.2082, and DESI-167.8517 + 14.1473, which are 151 pixels ≈40″3 on the side.

human inspection. The Legacy Surveys data is cataloged by Tractor and organized in folders, with each folder corresponding to one degree of R.A. on the sky. The efficiency of our trained ResNet is highly uneven. The number of ResNet-recommended objects per folder in the probability >0.9 bin vary from under 200 to over 3000. We have examined folders with both small and large numbers of objects. In general the folders with lower numbers of objects have higher purity.

We illustrate this trend in Figure 10, by using the number of passes for z-band as a proxy for depth (as in Figure 1). The left panel (orange columns) shows that while ~5% of the objects in the 10+ pass bin receive probability >0.9 ("recommendations"),
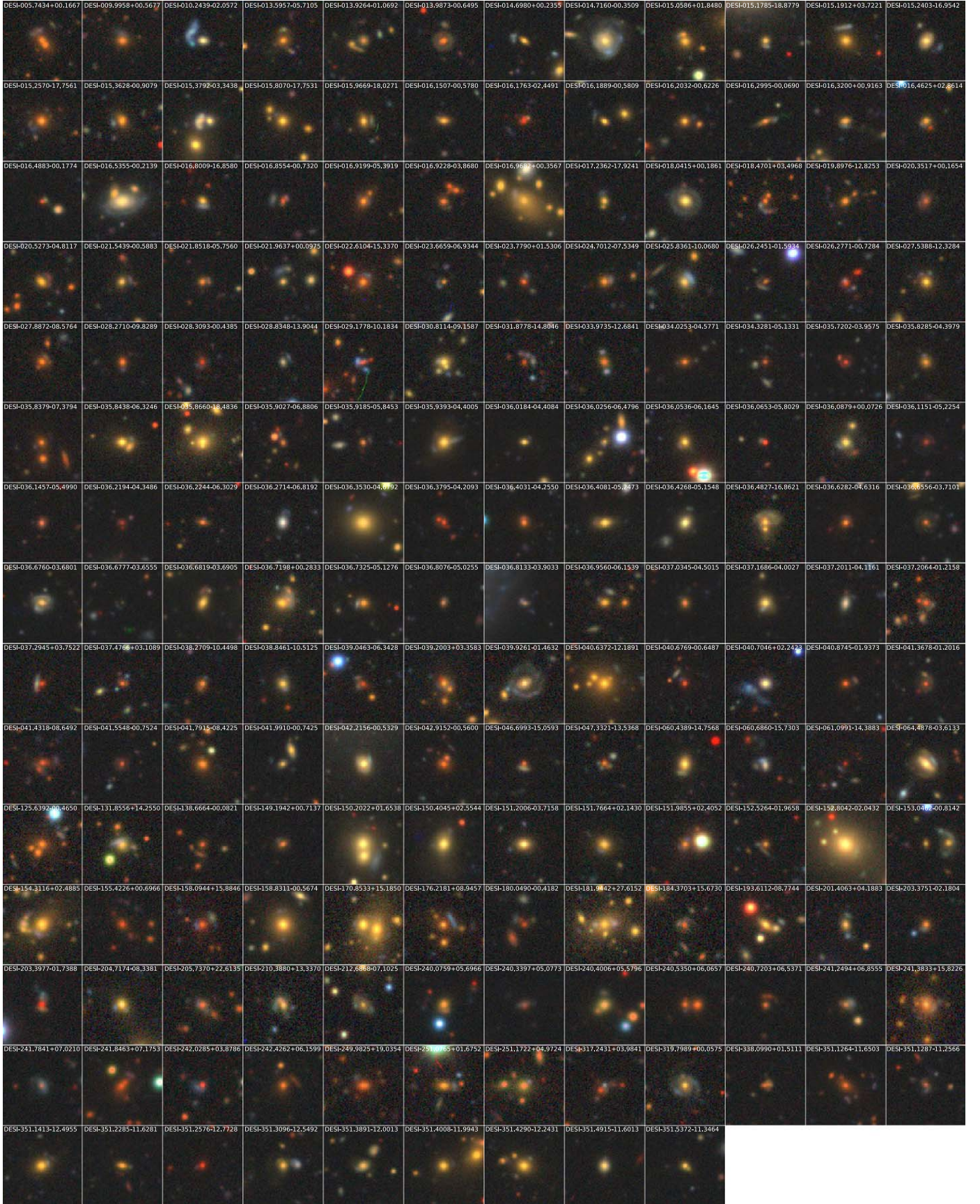
Figure 6. 176 Grade C lens candidates. Each image is 101 pixels $\approx 26{''}2$ on the side, with N up and E to the left.
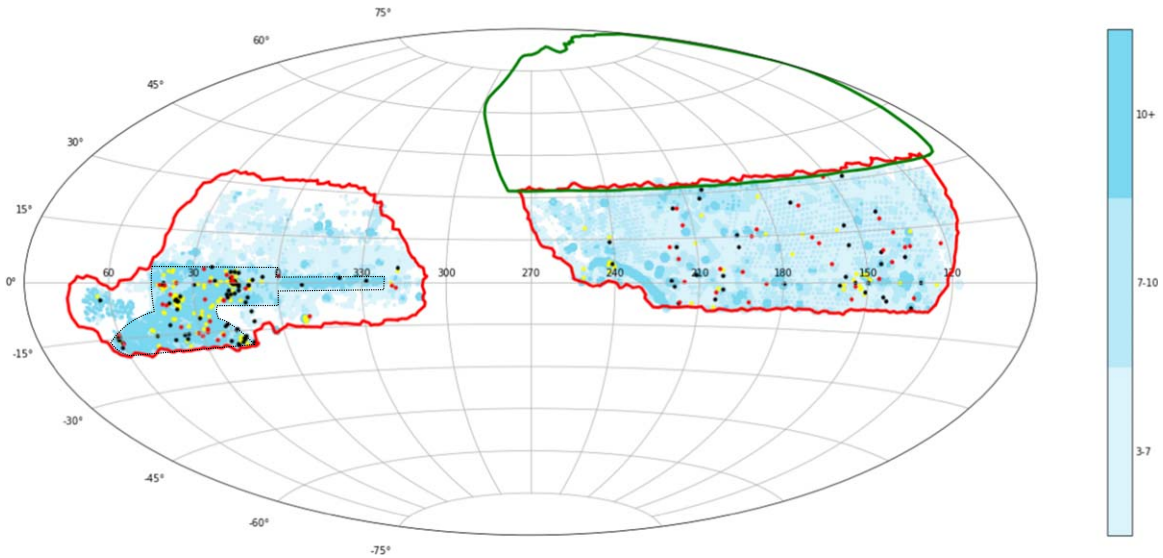
Figure 7. New candidate lensing systems identified in the DECaLS region are shown as red (Grade A), black (Grade B), and yellow (Grade C) circles. The footprint of DECaLS is highlighted by red outlines and the *z*-band depth is represented by different shades of blue (for more details, see the caption for Figure 1).
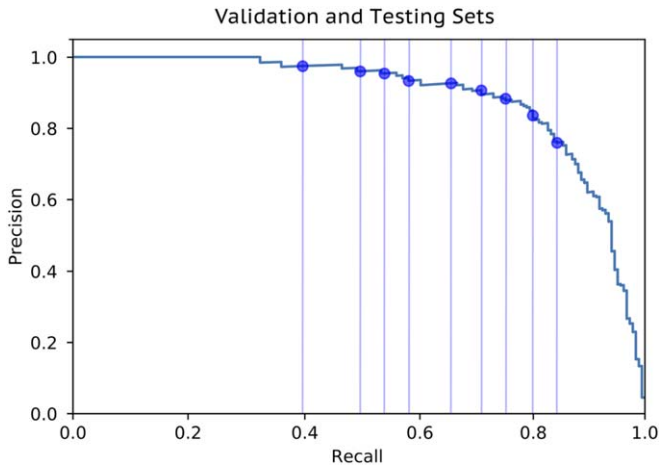
Figure 8. Precision-recall curve for the validation and testing sets. The blue points from left to right correspond to probability threshold values from 0.9 to 0.1 with an interval of 0.1.

Figure 9. Four examples of lensing systems where the blue arcs are very hard to tell, if at all, from DECaLS images, either due to their shallower *g*-band depth and/or slightly worse seeing (the deflection angle of the system in Panel (d) is $\sim 0\rlap{.}''5$). The systems shown in Panels (a)–(c) are from the Strong Lensing Legacy Survey, and the one in (d), the Hyper Suprime-Cam Subaru Strategic Program (see text).

only $\sim 0.1\%$ in the 3–7 passes bin do. There are certainly more lenses to be found in the deeper regions, but not 50 times more likely. Human inspection in fact reveals that a much lower percentage of the recommendations from the deepest bin are lens candidates (0.35%), compared with the shallower ones (0.45% for 7–10 passes and 1.61% for 3–7 passes; Figure 10, left panel, gray columns). The ResNet's preference for images with greater depth is also shown in the middle panel of Figure 10: while over 50% of the objects (blue column) are from the shallowest bin (3–7 passes), the fraction of recommendations is just below 20% (orange column); in contrast, objects from the deepest bin (10+ passes) only account for $\sim 5\%$ of the objects and yet over 80% of the recommendations are from this bin (again, blue and orange columns, respectively).

This is not a surprise. Since lensed sources typically are faint, most of the lenses in our training sample are in regions of greater depth (Figure 11, left panel; Figure 10, right panel, violet columns). The non-lenses in the training sample are mostly selected from shallower regions (Figure 11, right panel;

Figure 10, right panel, yellow columns). Such a training sample leads the ResNet to assign probabilities not only based on how likely an image contains a lensing system but also its depth. Note that in Figure 10, Panel (c), there is a small fraction of lenses in the training sample with fewer than three passes. Due to the small number of known lenses, we wanted to include as many lenses as possible.

We have found that the way to address this confusion is to include deep non-lens images. We will perform a full search for DR8, which was completed during the peer review process for
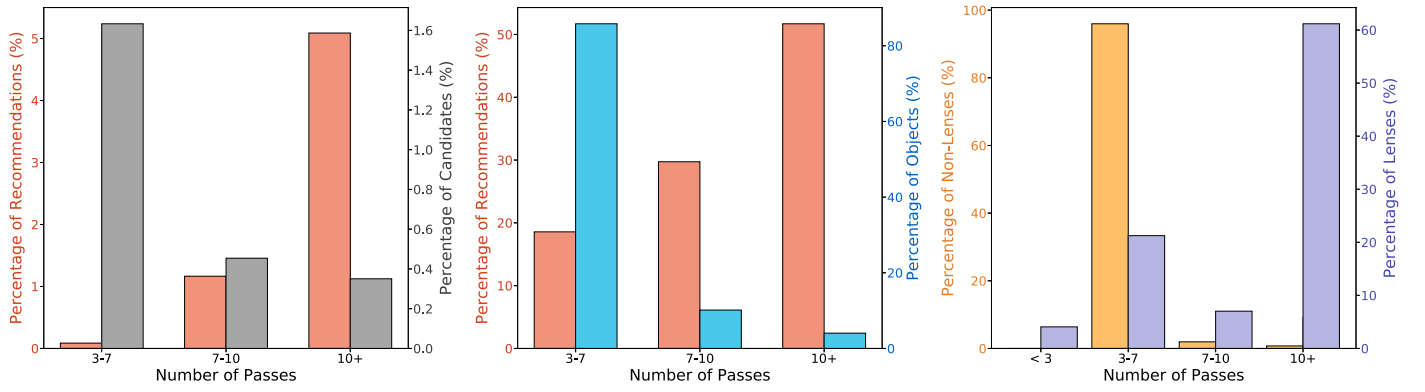
Figure 10. Left: orange columns (left *y*-axis) show the percentages of objects given a greater than 0.9 probability by our ResNet model (or "recommendations") for the three bins of *z*-band depth. The gray columns (right *y*-axis) show the percentages of ResNet recommendations that are selected as lens candidates through human inspection. Center: orange columns (left *y*-axis) show the percentages of ResNet recommendations for each bin of *z*-band depth. The blue columns (right *y*-axis) show the percentage of objects in each bin. These two panels show that the ResNet favors images with greater depth whether they contain a lensing system or not. This is a consequence of the composition of our current training sample, as shown in the last panel. Right: yellow (left *y*-axis) and violet (right *y*-axis) columns show the percentages of lenses and non-lenses in the training sample, respectively. Overall the images containing lensing systems tend to be much deeper, though a small fraction of them are shallower (see text). It is not a surprise that with such a training sample, we get the distributions of the recommendations and candidates relative to the depth seen in the first two panels.
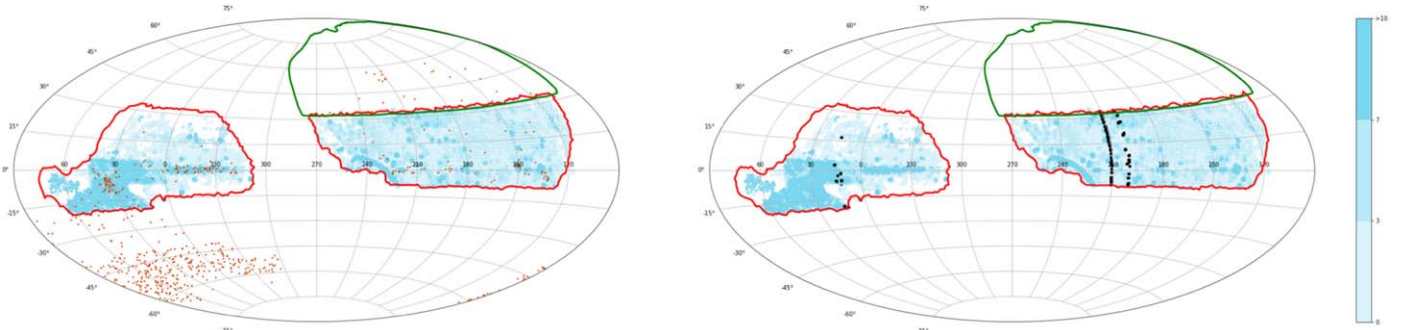
Figure 11. Lenses (red dots, left panel) and non-lenses (black dots, right panel) in our training sample, against the background of the depth map of DECaLS DR7 (see the caption for Figure 1). The lenses outside the DECaLS footprint are from DES, all with similar depth (10+ passes in *z* band).

this paper, using a larger and more statistically representative training sample (for more details, see Section 5.1).

5. Discussion

Our results so far are encouraging. In our current training sample we have only used 423 lenses. This is generally considered too small a number for a deep neural net. Nevertheless, we have succeeded in finding hundreds of new lens candidates over a large area of the sky for cutout images centered on elliptical galaxies. Here we will identify where we can improve.

For DR7, we have inspected the ResNet recommendations for approximately 3/4 of the sky for the DEV and COMP objects. For the remaining 1/4 of the folders, the number of recommendations are all high ($\gtrsim$1000/folder), which, as mentioned in Section 4.3, typically translates to low human inspection efficiency. We have stopped human inspection for now.

Based on our experience so far, we believe we can build a much better training sample, retrain, and deploy for DR8, which, as mentioned earlier, were completed during the referee process for this paper. The coverage and depth map for DR8 are shown in Figure 12. Note that there are patches where DR7 for DECaLS is deeper than DR8. This is because it is desirable that DR8 has a more uniform coverage.

5.1. Toward a Better Training Sample

We plan to take the following steps to improve our training sample. We need a larger non-lens sample (there are 13,000 in the current training sample) that will cover a greater variety of image configurations and, as mentioned in the previous section, include deep non-lens images. In our experience, having a large number of non-lenses is very helpful in terms of giving the neural net a better chance to reject a diverse variety of non-lenses. This experience comports with what has been reported by other authors. Metcalf et al. (2019) used 20,000 simulated non-lenses in the Lens Competition, which do not include the many complications arising in real observations. Jacobs et al. (2019) used 130,000 non-lenses in their training sample for an ensemble of CNN models to find high-redshift lenses in DES. As stated in Section 3, so far we have not used the validation and testing sets in our training. We have ~600 lenses in the entire current training sample. We can add ~160 lens candidates with high confidence, including all Grade A and Grade B candidates in this paper. Thus we will have ~760 lenses in our next training sample, ~80% more lenses than used for the current trained model.

In addition, we will make sure to include the following (many of these have been given greater than 0.9 probability of being a lens by the current trained ResNet model): star clusters; instances of interacting galaxies, ring galaxies, and more
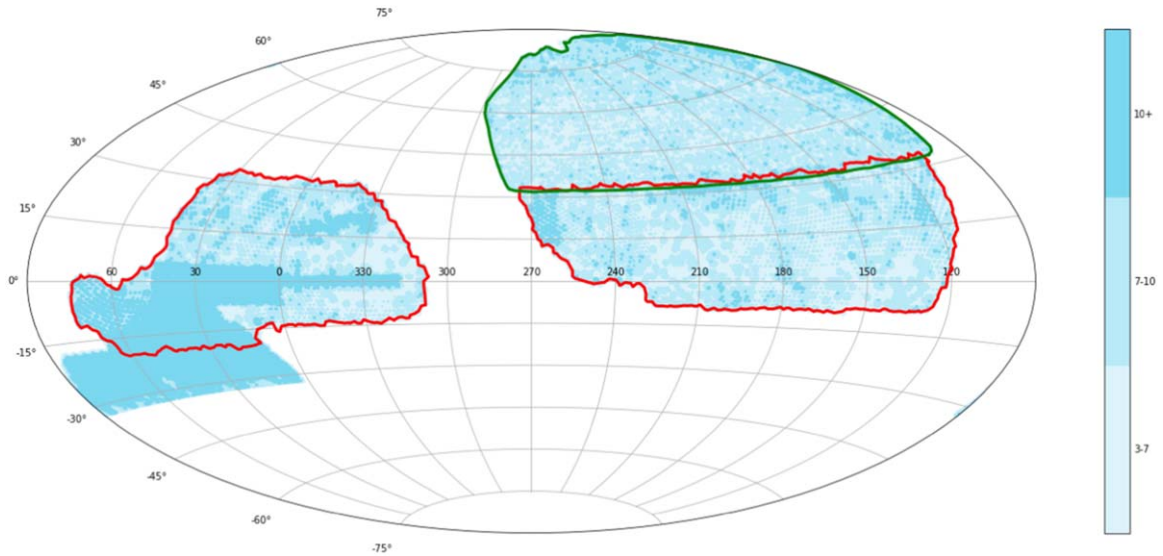
Figure 12. Coverage and depth map for DR8 of the Legacy Surveys. Below the Galactic plane, the footprint extends further south than DR7 (red outline), all of which overlaps with DES (also see Figure 1). Note that this map includes the MzLS/BASS region. Color scheme for number of passes is the same as in Figure 1.

varieties of spiral galaxies than in the current training sample; and more cosmic-ray examples, especially those in the bluest (*g*) band and those with curved and/or thick tracks.

During the peer review process, we have switched our training to graphics processing units and it is clear that the ResNet can train on a much larger sample within a reasonable amount of time. Though at this stage we have left the architecture and hyperparameters of the ResNet from L18 unchanged, we may vary both to optimize performance.

5.2. The MzLS/BASS Region

The logical next step is to search for lensing systems in the northern MzLS/BASS region for the DEV and COMP categories. In our current training sample, there are 21 lenses from the MzLS/BASS region, which have worse seeings in *gr* bands. Here we briefly discuss the performance of our current model in this region. Out of a total of the eight lenses in the validation and testing sets (4 each) in MzLS/BASS, a total of three (one in validation and two in testing) have probabilities >0.9, or 37.5%. This is remarkably similar to the 40% completeness for DECaLS. Of course, this is an estimate based on small numbers. Nevertheless it provides a sense of the level of completeness for lenses discoverable in the MzLS/BASS region if we deploy our current trained model. Efforts to adapt our model to this region, to account for the different seeing in *gr* bands and therefore possibly improve the performance of the ResNet model, is under way.

5.3. Lenses in the Tractor Galaxy Category of "REX"

The largest number of galaxies, by far, in the Legacy Surveys catalog are classified as the morphological type REX, i.e., the best-fit source model has a round exponential profile. The REX category contains an order of magnitude more objects than the DEV and COMP types combined, since most faint, extended galaxies are modeled by the REX profile. It likely includes many elliptical galaxies, though the percentage is unknown. Even so, given the total number of objects in this category is much larger than those in DEV and COMP

categories, there will likely be a large number of lensing systems to be discovered. Among the 199 known lenses from the Legacy Surveys in the training sample, 18 are typed as REX. Out of these, 12 have $z < 20.0$ mag and 1 with $z = 20.2$ mag. We will run inference on this category and report the results in a follow-up publication for lens search in DR8.

6. Conclusions

We have carried out a proof of concept end-to-end implementation of applying a deep residual neural network developed by Lanusse et al. (2018), trained on observed lenses and non-lenses, to a subset of the Legacy Surveys data: 5.7 million elliptical galaxies from DECaLS with a *z*-band magnitude cut of 20.0 mag. We use only real observations for training. In total, we have found 60 Grade A candidates (of these, 53 are new), 106 Grade B, and 176 Grade C candidates (all new).

The results are promising. Despite using a relative small training set with 423 lens and 9451 non-lenses for a survey with non-uniform depth (given that the survey was not yet completed), in this paper we report the discovery of the first batch of 335 new strong lens candidates from the Legacy Surveys. We will improve our training sample and model for the next round of training for full deployment on the entire Legacy Surveys DR8 footprint.

ORCID iDs

X. Huang ⬤ https://orcid.org/0000-0001-8156-0330
D. J. Schlegel ⬤ https://orcid.org/0000-0002-5042-5088
A. Dey ⬤ https://orcid.org/0000-0002-4928-4003
S. Juneau ⬤ https://orcid.org/0000-0002-0000-2394
M. Landriau ⬤ https://orcid.org/0000-0003-1838-8528
D. Lang ⬤ https://orcid.org/0000-0002-1172-0754
A. Meisner ⬤ https://orcid.org/0000-0002-1125-7384
E. F. Schlafly ⬤ https://orcid.org/0000-0002-3569-7421
F. Valdes ⬤ https://orcid.org/0000-0001-5567-1301
J. Yang ⬤ https://orcid.org/0000-0001-5287-4242

References

Aihara, H., Armstrong, R., Bickerton, S., et al. 2018, PASJ, 70, S8
Blandford, R. D., & Narayan, R. 1992, ARA&A, 30, 311
Blanton, M. R., Bershady, M. A., Abolfathi, B., et al. 2017, AJ, 154, 28
Bolton, A. S., Burles, S., Koopmans, L. V. E., Treu, T., & Moustakas, L. A. 2006, ApJ, 638, 703
Bonvin, V., Courbin, F., Suyu, S. H., et al. 2017, MNRAS, 465, 4914
Brownstein, J. R., Bolton, A. S., Schlegel, D. J., et al. 2012, ApJ, 744, 41
Cabanac, R. A., Alard, C., Dantel-Fort, M., et al. 2007, A&A, 461, 813
Capak, P., Aussel, H., Ajiki, M., et al. 2007, ApJS, 172, 99
Carrasco, M., Barrientos, L. F., Anguita, T., et al. 2017, ApJ, 834, 210
de Jong, J. T. A., Verdoes Kleijn, G. A., Boxhoorn, D. R., et al. 2015, A&A, 582, A62
Despali, G., Vegetti, S., White, S. D. M., Giocoli, C., & van den Bosch, F. C. 2018, MNRAS, 475, 5424
Dey, A., Rabinowitz, D., Karcher, A., et al. 2016, Proc. SPIE, 9908, 99082C
Dey, A., Schlegel, D. J., Lang, D., et al. 2019, AJ, 157, 168
Diehl, H. T., Buckley-Geer, E. J., Lindgren, K. A., et al. 2017, ApJS, 232, 15
Eisenstein, D. J., Weinberg, D. H., Agol, E., et al. 2011, AJ, 142, 72
Flaugher, B., Diehl, H. T., Honscheid, K., et al. 2015, AJ, 150, 150
Gladders, M. D., Hoekstra, H., Yee, H. K. C., Hall, P. B., & Barrientos, L. F. 2003, ApJ, 593, 48
Goldstein, D. A., & Nugent, P. E. 2017, ApJL, 834, L5
Goldstein, D. A., Nugent, P. E., & Goobar, A. 2019, ApJS, 243, 6
Goldstein, D. A., Nugent, P. E., Kasen, D. N., & Collett, T. E. 2018, ApJ, 855, 22
Goobar, A., Amanullah, R., Kulkarni, S. R., et al. 2017, Sci, 356, 291
He, K., Zhang, X., Ren, S., & Sun, J. 2015a, arXiv:1512.03385
He, K., Zhang, X., Ren, S., & Sun, J. 2015b, arXiv:1502.01852
He, K., Zhang, X., Ren, S., & Sun, J. 2016, arXiv:1603.05027
Jacobs, C., Collett, T., Glazebrook, K., et al. 2019, MNRAS, 484, 5330
Jacobs, C., Glazebrook, K., Collett, T., More, A., & McCarthy, C. 2017, MNRAS, 471, 167
Kelly, P. L., Filippenko, A. V., Burke, D. L., et al. 2015, Sci, 347, 1459
Kochanek, C. S. 1991, ApJ, 373, 354
Koopmans, L. V. E., & Treu, T. 2002, ApJL, 568, L5
Koopmans, L. V. E., Treu, T., Bolton, A. S., Burles, S., & Moustakas, L. A. 2006, ApJ, 649, 599
Kubo, J. M., Allam, S. S., Annis, J., et al. 2009, ApJL, 696, L61
Lang, D., Hogg, D. W., & Mykytyn, D. 2016, The Tractor: Probabilistic Astronomical Source Detection and Measurement, v. dr7.0, Astrophysics Source Code Library, ascl:1604.008
Lanusse, F., Ma, Q., Li, N., et al. 2018, MNRAS, 473, 3895
Lynds, R., & Petrosian, V. 1986, BAAS, 18, 1014
Metcalf, R. B., Meneghetti, M., Avestruz, C., et al. 2019, A&A, 625, A119
More, A., Cabanac, R., More, S., et al. 2012, ApJ, 749, 38
Moustakas, L. A., Brownstein, J., Fadely, R., et al. 2012, AAS Meeting Abstracts, 219, 146.01
Oguri, M., & Marshall, P. J. 2010, MNRAS, 405, 2579
Paczynski, B. 1987, Natur, 325, 572
Petrillo, C. E., Tortora, C., Chatterjee, S., et al. 2017, MNRAS, 472, 1129
Pourrahmani, M., Nayyeri, H., & Cooray, A. 2018, ApJ, 856, 68
Quimby, R. M., Oguri, M., More, A., et al. 2014, Sci, 344, 396
Refsdal, S. 1964, MNRAS, 128, 307
Ritondale, E., Vegetti, S., Despali, G., et al. 2019, MNRAS, 485, 2179
Sharon, K., Bayliss HÅkon Dahle, M. B., Dunham, S. J., et al. 2020, MNRAS, 247, 12
Sonnenfeld, A., Chan, J. H. H., Shu, Y., et al. 2018, PASJ, 70, S29
Soucail, G., Fort, B., Mellier, Y., & Picat, J. P. 1987, A&A, 172, L14
Soucail, G., Mellier, Y., Fort, B., Mathez, G., & Cailloux, M. 1988, A&A, 191, L19
Stark, D. P., Auger, M., Belokurov, V., et al. 2013, MNRAS, 436, 1040
Suyu, S. H., Auger, M. W., Hilbert, S., et al. 2013, ApJ, 766, 70
Suyu, S. H., Marshall, P. J., Auger, M. W., et al. 2010, ApJ, 711, 201
Tessore, N., Bellagamba, F., & Metcalf, R. B. 2016, MNRAS, 463, 3115
The Dark Energy Survey Collaboration 2005, arXiv:astro-ph/0510346
Treu, T., & Marshall, P. J. 2016, A&ARv, 24, 11
Tzeng, E., Hoffman, J., Saenko, K., & Darrell, T. 2017, arXiv:1702.05464
Vegetti, S., & Koopmans, L. V. E. 2009, MNRAS, 400, 1583
Walsh, D., Carswell, R. F., & Weymann, R. J. 1979, Natur, 279, 381
Williams, G. G., Olszewski, E., Lesser, M. P., & Burge, J. H. 2004, Proc. SPIE, 5492, 787
Wojtak, R., Hjorth, J., & Gall, C. 2019, MNRAS, 487, 3342
Wong, K. C., Sonnenfeld, A., Chan, J. H. H., et al. 2018, ApJ, 867, 107
Wong, K. C., Suyu, S. H., Chen, G. C. F., et al. 2019, arXiv:1907.04869
York, D. G., Adelman, J., Anderson, J. E., Jr., et al. 2000, AJ, 120, 1579